$Gd_{12}Co_{5.3}Bi$ and $Gd_{12}Co_5Bi$, Crystalline Doppelgänger with Low Thermal Conductivities

Anton O. Oliynyk,[†] Taylor D. Sparks,[‡] Michael W. Gaultois,[§] Leila Ghadbeigi,[‡] and Arthur Mar[†,*]

[†] *Department of Chemistry, University of Alberta, Edmonton, AB T6G 2G2 Canada*

[‡] *Department of Materials Science and Engineering, University of Utah, Salt Lake City, UT 84112 USA*

[§] *Department of Chemistry, University of Cambridge, Cambridge CB2 1EW United Kingdom*

Abstract

Attempts to prepare $Gd_{12}Co_5Bi$, a member of the rare-earth intermetallics $RE_{12}Co_5Bi$, which have been identified by a machine-learning recommendation engine as potential candidates for thermoelectric materials, led instead to formation of the new compound $Gd_{12}Co_{5.3}Bi$ with a very similar composition. Phase equilibria near the Gd-rich corner of the Gd–Co–Bi phase diagram were elucidated by both lab-based and variable-temperature synchrotron powder X-ray diffraction, suggesting that $Gd_{12}Co_{5.3}Bi$ and $Gd_{12}Co_5Bi$ are distinct phases. The higher symmetry structure of $Gd_{12}Co_{5.3}Bi$ (cubic, space group $Im\bar{3}$, Z = 2, a = 9.713(6) Å), as determined from single-crystal X-ray diffraction, is closely related to that of $Gd_{12}Co_5Bi$ (tetragonal, space group *Immm*). Single Co atoms and Co–Co dumbbells are disordered with occupancies of 0.78(2) and 0.22(2), respectively, in $Gd_{12}Co_{5.3}Bi$, but they are ordered in $Gd_{12}Co_5Bi$. Consistent with this disorder, the electrical resistivity shows less dependence on temperature for $Gd_{12}Co_{5.3}Bi$ than for $Gd_{12}Co_5Bi$. The thermal conductivity is low and reaches 2.8 W m^{-1} K^{-1} at 600 °C for both compounds; however, the temperature dependence of the thermal conductivity differs, decreasing for $Gd_{12}Co_{5.3}Bi$ and increasing for $Gd_{12}Co_5Bi$ as the temperature increases. The unusual trends in thermal properties persist in the heat capacity, which decreases below 2*R*, and in the thermal diffusivity, which increases at higher temperatures.

Keywords: Rare-earth intermetallics; Crystal structure; Order-disorder phenomena; Thermal properties

1. Introduction

Ternary phases in the rare-earth transition-metal bismuth systems *RE*–*M*–Bi remain poorly investigated because of considerable problems in synthesis and structural characterization, which are hindered by difficulties in crystal growth and severe X-ray absorption.[1] A decade ago, Tkachuk and Mar reported an extensive series of rare-earth intermetallic compounds $RE_{12}Co_5Bi$ (*RE* = Y, Gd–Tm), which adopt a complex tetragonal structure mimicking nearly cubic symmetry, as determined from synchrotron powder X-ray diffraction data.[2] Careful examination of phase equilibria in the Ho–Co–Bi system confirmed that $Ho_{12}Co_5Bi$ is distinct from Ho_5Co_2Bi, another ternary phase that has a similar composition and closely related structure.[3] As anticipated by the strong coupling of f-electrons from the *RE* atoms and d-electrons from the Co atoms, many $RE_{12}Co_5Bi$ members display complex magnetic behaviour with multiple ordering transitions, as revealed by magnetic susceptibility measurements and μSR spectroscopy.[1,4–7]

Surprisingly, $RE_{12}Co_5Bi$ compounds were recently suggested through data mining methods to be potential candidates for thermoelectric materials.[8] This is counterintuitive because intermetallic compounds with a high proportion of f- and d-elements are completely outside the realm of normal chemical compositions for thermoelectrics. Highly metallic phases typically have low Seebeck coefficients, which would lead to poor thermoelectric figures of merit unless there were other compensating properties (high electrical conductivity, low thermal conductivity) to make testing worthwhile, as suggested by the machine-learning recommendation engine. In agreement with predictions, $Gd_{12}Co_5Bi$ and $Er_{12}Co_5Bi$ were found to exhibit low thermal conductivities (4–8 W m^{-1} K^{-1}), comparable to half-Heusler phases.[8] Moreover, the thermal conductivity of these compounds increases as temperature increases, a dependence that is

contrary to expectations. According to the Wiedemann-Franz law, $\kappa_e = L\sigma T$, the electronic contribution to the thermal conductivity is proportional to the electrical conductivity and temperature; for metals, conductivity effects strongly correlate with free electrons and the electrical conductivity decreases with higher temperature as their mean free paths shorten. At intermediate temperatures, the phonon contribution to the thermal conductivity also decreases with higher temperature as Umklapp scattering is enhanced with greater population of phonons. Therefore, almost all materials, and certainly metals, should exhibit thermal conductivity which decreases as a function of increasing temperature, raising the question as to the origin of the reversed trend of increasing thermal conductivity observed for $RE_{12}Co_5Bi$. Such an unusual property may have interesting applications for thermal rectification, in which two materials with opposing temperature dependences of the thermal conductivity can be combined to create a device that acts like a thermal diode.[9]

As part of renewed efforts to further examine the properties of $RE_{12}Co_5Bi$, it is essential to prepare samples in the form of phase-pure powders or single crystals, to elucidate the experimental conditions for optimizing synthesis, and to identify any possible impurities that could affect the interpretation of physical measurements. In particular, we wished to confirm the structure of $RE_{12}Co_5Bi$ through single-crystal methods, which are more accurate than the powder diffraction methods and which can provide more detailed information about anisotropic displacement parameters to gain insight on the unusually low thermal conductivity of these compounds. In the course of these investigations, crystals of what was believed to be $Gd_{12}Co_5Bi$ were analyzed by single-crystal X-ray diffraction. We report here an unanticipated outcome of this analysis, namely the existence of a new ternary phase, $Gd_{12}Co_{5.3}Bi$. It would be predicted (from the machine-learning recommendation engine) to have similar properties to $Gd_{12}Co_5Bi$ – a

high probability of exhibiting high electrical conductivity and low thermal conductivity, but a low probability of exhibiting high Seebeck coefficient. Like Dostoyevsky's *dvoynik*,[10] $Gd_{12}Co_{5.3}Bi$ resembles its counterpart with nearly the same composition, $Gd_{12}Co_5Bi$, but exhibits subtle differences in structure and properties.

2. Experimental Section

2.1. Crystal Growth. *2.1.1. Use of Fluxes.* Stoichiometric mixtures of the elements with loading composition $Gd_{12}Co_5Bi$ and total mass of 0.5 g were prepared from freshly filed Gd pieces (99.9%, Hefa), Co powder (99.99%, Alfa-Aesar), and Bi pieces freshly ground to powders (99.999%, Cerac). The mixtures were pressed into pellets and each combined with various metal fluxes having low melting points (Bi, Pb, Sn, In, Ga) in a mass ratio of 1:10. A sixth reaction was prepared by combining a pellet of loading composition $Gd_{12}Co_5Bi$ with a NaCl–KCl (1:1 by mass) flux in a mass ratio of 1:1. These mixtures were each placed within fused-silica tubes which were evacuated and sealed. For the reaction containing NaCl–KCl flux, the tube was carbon-coated through pyrolysis of ethanol prior to loading. The tubes were heated in a furnace to 1000 °C within 8 h, held at this temperature for 1 h, and slowly cooled down at a rate of 2 °C/h. The tubes containing metal fluxes were removed from the furnace when the temperature reached 50 °C above the melting point of the metal, at which point the molten flux was centrifuged. The tube containing the NaCl–KCl flux was cooled to room temperature (and the flux was removed by washing with water). A parallel set of reactions was conducted containing the same six fluxes except that the charge consisted of the actual ternary phase $Gd_{12}Co_5Bi$, which was prepared by arc-melting (see below). In all cases, no crystals of

$Gd_{12}Co_5Bi$ were obtained; any crystals that formed were found to be binary phases from the Gd–In, Gd–Sn, or Gd–Co systems.

2.1.2. Use of Iodine. A stoichiometric mixture of the elements was pressed into a pellet as before and combined with a small amount of I_2 (~30 mg) within a 20-cm-long fused-silica tube. The tube was evacuated, sealed, and placed within a furnace heated gradually to 800 °C, which is above the melting point of $Gd_{12}Co_5Bi$, held at this temperature for 2 d, and slowly cooled down to room temperature at a rate of 5 °C/h. The tube was positioned such that the end containing the charge was at the centre of the furnace and the other end was near the edge of the furnace. The tube furnaces within our laboratory have been previously calibrated and found to exhibit good uniformity, with a temperature gradient of <3 °C between the centre and edge of the furnace. Agglomerations of small crystals were found embedded on an ingot substrate, as seen in an image obtained on a JEOL JSM-6010LA scanning electron microscope (Figure 1). These crystals were identified to be the new phase, $Gd_{12}Co_{5.3}Bi$, and were selected for single-crystal X-ray diffraction analysis. The remaining ingot was mostly Gd_5CoBi_2, as confirmed by EDX analysis and its reactivity with water.

2.2. Phase Equilibria. In light of the discovery of $Gd_{12}Co_{5.3}Bi$ crystals from the use of iodine as described above, further reactions involving arc-melting were conducted in attempts to prepare bulk material and to elucidate phase equilibria. Pressed pellets of mixtures of the elements were prepared with various loading compositions in the vicinity of the compositions $Gd_{12}Co_{5.3}Bi$ and $Gd_{12}Co_5Bi$ within the ternary phase diagram. A small excess (2% by mass) of Bi, which has a high vapour pressure, was added to compensate for anticipated loss of Bi. Each pellet was placed on a water-cooled copper hearth in an Edmund Bühler MAM-1 arc-melter. The chamber was evacuated and backfilled with argon gas, and the procedure was repeated. Any

trace oxygen was removed by melting a Ti getter first, before the arc was redirected to melt the sample. To ensure homogeneity, each sample was melted a second time after it was flipped. The arc-melted ingots were then placed within evacuated and sealed fused-silica tubes, annealed in a furnace at 600 °C for 1 week, and quenched in cold water. Ground samples were analyzed by powder X-ray diffraction (XRD) with Cu $K\alpha_1$ radiation on an Inel diffractometer equipped with a curved position-sensitive detector (CPS 120). Polished samples embedded in resin were examined by energy-dispersive X-ray (EDX) analysis on a JEOL JSM-6010LA scanning electron microscope. The samples were largely homogeneous but interrupted by quite small inclusions of minor phases (estimated at less than 5 mol. %) (Figure S1 in Supporting Information). Because the uncertainties in the EDX analyses were larger than the difference in composition between $Gd_{12}Co_5Bi$ (observed 69(2)% Gd, 26(2)% Co, 5(2)% Bi; expected 67% Gd, 28% Co, 5% Bi) and $Gd_{12}Co_{5.3}Bi$ (observed 66(3)% Gd, 28(2)% Co, 6(2)% Bi; expected 66% Gd, 29% Co, 5% Bi), XRD analysis was absolutely essential to characterize these two ternary phases.

To confirm the phase equilibria and to compare the thermal stability of $Gd_{12}Co_5Bi$ and the new compound $Gd_{12}Co_{5.3}Bi$, which were difficult to distinguish from the laboratory-based powder XRD patterns, further high-resolution synchrotron X-ray diffraction experiments were performed on beamline 11-BM at the Advanced Photon Source (APS) at Argonne National Laboratory. The samples for the synchrotron experiments were ground down to fine powder and sealed into Kapton tubes. The wavelength of X-rays used was 0.413905 Å for $Gd_{12}Co_5Bi$, 0.459300 Å for $Gd_{12}Co_{5.3}Bi$, or 0.414208 Å for two-phase samples. Fitting of the XRD patterns for the $Gd_{12}Co_5Bi$ and $Gd_{12}Co_{5.3}Bi$ samples confirmed that they are nearly single-phase,

consistent with the EDX results (Figure S2 in Supporting Information). Variable-temperature X-ray diffraction patterns were collected at 100 K, 200 K, 295 K (or 300 K), 400 K, and 475 K.

2.3. Structure Determination. Two crystals of what was eventually determined to be $Gd_{12}Co_{5.3}Bi$ were selected for single-crystal X-ray diffraction analysis. As similar results were obtained, we present data for only one of these crystals. Intensity data were collected at room temperature on a Bruker PLATFORM diffractometer equipped with a SMART APEX II CCD area detector and a graphite-monochromated Mo $K\alpha$ radiation source, using ω scans at 8 diffferent ϕ angles with a frame width of 0.3° and an exposure time of 20 s per frame. Face-indexed absorption corrections were applied. Structure solution and refinement were carried out with use of the SHELXTL (version 6.12) program package.[11] The centrosymmetric cubic space group $Im\overline{3}$ was chosen on the basis of Laue symmetry, systematic absences, and intensity statistics. Direct methods revealed initial positions for Gd at 24*g*, Co at 12*e*, and Bi at 2*a*, which corresponds to two formula units of "$Gd_{12}Co_6Bi$". Refinement of this model, with anisotropic displacement parameters included, proceeded normally but the agreement factors remained somewhat high (R_1 = 0.071) and the difference map revealed significant residual electron density ($(\Delta\rho)_{max}$ = 17.8 $e^-/Å^3$, $(\Delta\rho)_{min}$ = –4.2 $e^-/Å^3$). This electron density is located at 6*b* (0, ½, ½), at the midpoint between a pair of existing Co atoms (0, ½, 0.12 and 0, ½, 0.88). We proposed to assign this new site at 6*b* as Co2, and relabeled the previous site at 12*e* as Co1. The interpretation of this model is that there is disorder between Co1–Co1 dumbbells and single Co2 atoms. Refinements in which the occupancies of these sites were constrained to sum to unity led to 0.78(2) in the Co1 site and 0.22(2) in the Co2 site. The agreement factors were now satisfactory (R_1 = 0.049) and the difference map was featureless ($(\Delta\rho)_{max}$ = 4.1 $e^-/Å^3$, $(\Delta\rho)_{min}$ = –2.9 $e^-/Å^3$). The resulting formula, $Gd_{12}Co_{5.3(1)}Bi$, agrees with the loaded reaction composition

$Gd_{12}Co_{5.3}Bi$ (with 2% excess Bi added to compensate for vaporization losses) and the EDX analyses.

An alternative interpretation of the additional electron density peak at 6*b* is that it is a site partially occupied by Bi atoms instead of Co atoms, but this possibility can be ruled out for the following reasons. Most importantly, this model would contain extremely short Gd–Bi distances of 2.7 Å which are physically unrealistic; for comparison, the average Gd–Bi distance found in other compounds is 3.2 Å and the lower bound is 2.9 Å.[12] A refinement of this model led to a very low occupancy (0.08(1)) of Bi in this site, somewhat worse agreeement factors (R_1 = 0.052), and a formula ($Gd_{12}Co_{5.5}Bi_{1.2}$) that is inconsistent with the loaded reaction composition. Furthermore, no extraneous elements were found in the EDX analysis (Figure S1 in Supporting Information).

Crystallographic data, positional and displacement parameters, and interatomic distances are listed in Table 1. Further data in the form of a crystallographic information file (CIF) are available as Supporting Information.

2.4. Electrical Resistivity. Small bar-shaped pieces (with longest dimensions of 1 mm) were cut from an ingot confirmed to be essentially single-phase $Gd_{12}Co_{5.3}Bi$ by powder X-ray diffraction and EDX analyses. Standard four-probe electrical resistivity measurements were made between 2 and 300 K on a Quantum Design Physical Property Measurement System (PPMS) equipped with an ac transport controller (Model 7100). The current was 100 μA and the frequency was 16 Hz. Measurements conducted upon heating and cooling the same sample indicated relative errors of up to 4% in the absolute resistivity values; measurements on two samples differed by 10% in the absolute resistivity values.

2.5. Thermal Properties. Thermal conductivity, κ, of the samples was calculated from the standard relationship $\kappa = \rho\alpha C_p$, where ρ is the density, α is the thermal diffusivity, and C_p is the heat capacity at constant pressure. Density was measured via the Archimedes method with water at 20 °C as the immersion medium. Heat capacity was determined at the University of Utah using a Netzsch Sirius 3500 temperature modulated differential scanning calorimeter (TM-DSC). Small fragments were cut from the annealed arc-melted ingots of $Gd_{12}Co_5Bi$ and $Gd_{12}Co_{5.3}Bi$ and calorimetry measurements were performed on two samples of each compound from room temperature up to 600 °C under an inert atmosphere of Ar. The aluminum containers were not visibly affected during these measurements. The unusual temperature dependence of the heat capacity led us to repeat these measurements on the same samples on additional DSC instruments including a Perkin Elmer Pyris 1 DSC at the University of Alberta as well as through a third party analytical laboratory (Evans Analytical Group). Thermal diffusivity was measured on annealed arc-melted ingots. Samples were first polished to be coplanar with a thickness of 1 mm to 2 mm and then cut into disc shapes with either 8 mm or 12 mm diameters via electrical discharge machining. The density of the samples, evaluated by dividing the mass by the volume of these discs, was 97% (for $Gd_{12}Co_5Bi$) or 95% (for $Gd_{12}Co_{5.3}Bi$) of the theoretical density derived from the X-ray analysis. The thermal diffusivity of the discs was then measured using the laser flash method with a Netzsch LFA 457 instrument with a Cape-Lehman pulse length and heat loss correction model.[13] Samples were coated with graphite on both sides to promote uniform absorption and emission. Measurements were taken from room temperature up to 600 °C in 100 °C increments under an inert atmosphere of Ar. Powder XRD patterns of the samples were unchanged after these measurements.

3. Results and Discussion

With the original intent to grow crystals of $Gd_{12}Co_5Bi$, various fluxes and heating profiles were used, but all were unsuccessful. Surprisingly, use of iodine acting as a vapour transport agent led to formation of crystals, not of $Gd_{12}Co_5Bi$, but rather of a slightly different ternary phase $Gd_{12}Co_{5.3}Bi$. Given the close proximity of these compositions, it was thus important to clarify the phase equilibria taking place in the Gd–Co–Bi system, which was investigated by arc-melting and annealing samples at 600 °C. By analogy with the corresponding Ho–Co–Bi system studied earlier (at 800 °C), the most likely impurities in any preparation of $Gd_{12}Co_5Bi$ were initially anticipated to be phases in its vicinity, namely Gd_3Co, Gd_5CoBi_2, and $Gd_6Co_{4.5}$. The large proportion of heavy elements in these samples led to severe absorption in the powder XRD patterns, which generally showed suppressed intensities. If short data collection times were used (on a diffractometer equipped with a curved position-sensitive detector and Cu $K\alpha_1$ radiation), it was easy to confuse the XRD patterns of $Gd_{12}Co_5Bi$ and the new phase $Gd_{12}Co_{5.3}Bi$ by mistakenly attributing merged peaks to poor resolution. With increased data collection times to improve the signal-to-noise ratio, the XRD patterns of $Gd_{12}Co_5Bi$ and $Gd_{12}Co_{5.3}Bi$ were found to be distinguishable (Figures 2a–b). To augment these laboratory-based XRD data, higher-resolution XRD data obtained using synchrotron radiation confirmed that $Gd_{12}Co_5Bi$ and $Gd_{12}Co_{5.3}Bi$ have different patterns (Figures 2c–d). The fewer peaks in the pattern of $Gd_{12}Co_{5.3}Bi$ imply a higher symmetry than in $Gd_{12}Co_5Bi$.

To test the reproducibility of the synthesis, over 20 samples were prepared with the nominal composition $Gd_{12}Co_{5.3}Bi$ through arc-melting and annealing. Reassuringly, more than 90% of the samples resulted in the expected phase $Gd_{12}Co_{5.3}Bi$. The remaining samples indicated formation of $Gd_{12}Co_5Bi$, possibly as a result of deviations in composition caused by

small volatilization losses during arc-melting. Because all peaks in the powder XRD pattern for $Gd_{12}Co_{5.3}Bi$ occur as a subset of peaks for $Gd_{12}Co_5Bi$, with only small differences in intensities, it is virtually impossible to distinguish between samples containing solely $Gd_{12}Co_5Bi$ and those containing a mixture of the two phases from this technique alone. To avoid this situation, adding 3% excess Co shifts the composition just slightly to a three-phase region in the phase diagram (see below) where overwhelmingly $Gd_{12}Co_{5.3}Bi$ (instead of $Gd_{12}Co_5Bi$) and only minimal amounts of impurities (Gd_5CoBi_2, $Gd_6Co_{4.5}$) are formed. Conversely, slightly Co-poor compositions favour formation of $Gd_{12}Co_5Bi$.

The similarity of the formulas $Gd_{12}Co_5Bi$ and $Gd_{12}Co_{5.3}Bi$, which differ in composition by only 1–2 at. %, raises the question of whether these phases are merely polymorphic modifications that are stabilized at different temperatures, or if one of these is a metastable phase. When a sample of $Gd_{12}Co_5Bi$ was annealed further for one month at 600 °C, which is a very long period of time to ensure that equilibrium is attained, its powder XRD pattern remained unchanged. Identical treatment of a sample of $Gd_{12}Co_{5.3}Bi$ for the same duration at the same temperature also led to no changes. These results imply that $Gd_{12}Co_5Bi$ and $Gd_{12}Co_{5.3}Bi$ are distinct, both thermodynamically stable at 600 °C. High-resolution synchrotron XRD patterns collected on separate samples of $Gd_{12}Co_5Bi$ and $Gd_{12}Co_{5.3}Bi$ at variable temperatures from 100 K to 475 K (unfortunately, instrumental limitations did not permit experiments at higher temperatures) revealed no changes (Figures 2c–d), implying that $Gd_{12}Co_5Bi$ and $Gd_{12}Co_{5.3}Bi$ do not undergo structural transformations within this temperature range.

The phase diagram near the Gd corner of the Gd–Co–Bi system at 600 °C was elucidated in more detail through XRD and metallographic analyses of 8 samples; each sample was prepared twice to confirm reproducibility (Figure 3). Cell parameters for the binary and ternary

phases present in this diagram are listed in Table 2. Tie lines from $Gd_{12}Co_5Bi$ and $Gd_{12}Co_{5.3}Bi$ to neighbouring phases (Gd_5CoBi_2, Gd_3Co, and $Gd_6Co_{4.5}$) were established. For example, powder XRD patterns are shown for two-phase samples containing $Gd_{12}Co_5Bi$ and Gd_3Co (sample 3), $Gd_{12}Co_{5.3}Bi$ and Gd_5CoBi_2 (sample 5), and $Gd_{12}Co_{5.3}Bi$ and $Gd_6Co_{4.5}$ (sample 6) (Figure 4). As before, the lab-based XRD data suffered from severe absorption effects. However, additional high-resolution synchrotron XRD patterns with much cleaner backgrounds were collected for samples 5 and 6, which were confirmed to contain the phases initially identified from the lab-based data. The binary phase $Gd_6Co_{4.5}$ accommodates a modest solubility of the third component Bi, corresponding to the formula $Gd_6(Co_{1-x}Bi_x)_{4.5}$ (x = 0–0.15).

The cubic structure of $Gd_{12}Co_{5.3}Bi$ is easy to understand if it is first described in terms of a three-dimensional network of corner-sharing Gd_6 octahedra (Figure 5). This network is undoubtedly well known to readers familiar with the now popular skutterudite structure ($CoAs_3$-type),[14] adopted by transition-metal pnictides MPn_3 (M = Fe, Co, Rh, Ir, and others; Pn = P, As, Sb);[15,16] additional atoms can enter icosahedral voids between the M-centred Pn_6 octahedra to give rise to filled skutterudites AM_4Pn_{12} (A = alkali, alkaline-earth, and rare-earth metals).[17] The space group is $Im\bar{3}$ in both $Gd_{12}Co_{5.3}Bi$ and AM_4Pn_{12}. In $Gd_{12}Co_{5.3}Bi$, the centres of the Gd_6 octahedra are empty and the icosahedral voids are filled by Bi atoms. Within the cubic unit cell, the Gd_6 octahedra are located within each of the eight octants and the Bi atoms are located at the corners and centre. The complicating feature in $Gd_{12}Co_{5.3}Bi$ is the presence of split Co1 (at 12*e*) and Co2 sites (at 6*b*). The refined occupancies were 0.78(2) for Co1 and 0.22(2) for Co2. In other words, there is a superposition of two possible local atomic arrangements consisting of Co–Co dumbbells (with a rather short distance of 2.23(1) Å) and single Co atoms, located at the edges and faces of the cubic unit cell (Figure 6a). The electron density map determined from the

single-crystal XRD data clearly reveals maxima that support the presence of distinct sites as opposed to just a single site with elongated displacement parameters (Figures 6b–c).

An alternative way to describe the structure of $Gd_{12}Co_{5.3}Bi$ is to focus on the presence of Gd_4 squares. Although the Gd–Gd distances (3.826(4)–3.828(4) Å) are not the shortest in the structure, these Gd_4 squares draw attention to similar Pn_4 squares that appear in skutterudite. If the unit cell is translated by ¼, ¼, ¼, the Gd_4 squares are located within six of the eight octants of the cube, and Bi atoms occupy the remaining two octants (Figure 7a). The Co–Co dumbbells and Co atoms, as a disordered set, are centred within the Gd_4 squares. $Gd_{12}Co_{5.3}Bi$ shows a clear relationship to that of $Ho_{12}Co_5Bi$ (this is the name of the structure type adopted by $RE_{12}Co_5Bi$ compounds because a full crystal structure was determined for this particular member)[2] (Figure 7b). Here, there is an ordered arrangement of Co–Co dumbbells skewering four of the Gd_4 squares and Co atoms centering the remaining two Gd_4 squares.

The symmetry relationship between $Gd_{12}Co_{5.3}Bi$ and $Ho_{12}Co_5Bi$ structure types is concisely summarized in a Bärnighausen tree[18] (Figure 8). The evolution of $Gd_{12}Co_{5.3}Bi$ (space group $Im\bar{3}$) to $Ho_{12}Co_5Bi$ (space group *Immm*) proceeds through a *translationengleiche* reduction in symmetry of index 3. The tetragonal space group *Immm* (full Hermann-Mauguin symbol $I\ 2/m\ 2/m\ 2/m$) is a maximal non-isomorphic subgroup of the cubic space group $Im\bar{3}$ (full symbol $I\ 2/m\ \bar{3}$). That is, there is a loss of the threefold rotoinversion axes along the body diagonals of a cube. This symmetry reduction can be appreciated by noting that the Co–Co dumbbells can be aligned in all three directions along *a*, *b*, and *c* in $Gd_{12}Co_{5.3}Bi$, but only in two directions in $Ho_{12}Co_5Bi$ (Figure 7). Except for the Bi atoms, all atomic sites in $Gd_{12}Co_{5.3}Bi$ split into three sets of independent positions while retaining the local site symmetry on proceeding to $Ho_{12}Co_5Bi$. The Gd site at 24*g* splits into 8*l*, 8*m*, and 8*n*. The Co site

corresponding to the Co–Co dumbbells at 12*e* splits into 4*f*, 4*h*, and 4*j*, among which one of these is vacant in $Ho_{12}Co_5Bi$. The Co site accommodating single atoms at 6*b* splits into 2*b*, 2*d*, and 2*c*, among which two of these are vacant in $Ho_{12}Co_5Bi$.

Further relationships can be drawn to other structures, such as Ho_6Co_2Ga,[19] $Sm_{12}Ni_6In$,[20] and Ho_5Ni_2Sb,[21] as has been discussed previously,[2] by focusing on the stacking of 3^2434 and 4^4 nets and the occupation of sites between these nets. These structures are also characterized by dumbbells formed by the transition-metal component (Co–Co or Ni–Ni, with short distances of 2.2–2.3 Å) and sometimes there is a deficiency of these dumbbells, as occurs in $Dy_6Fe_{1.7}In$ (Ho_6Co_2Ga-type).[22] What sets $Gd_{12}Co_{5.3}Bi$ apart from these compounds is that it exhibits static disorder between Co–Co dumbbells and single Co atoms. This feature is reminiscent of other intermetallic compounds, such as RE_2Fe_{17} (containing Fe–Fe dumbbells and *RE* atoms)[23,24] and Fe_3Ge_2Sb (containing Sb–Sb dumbbells and Ge atoms)[25] in which the disorder occurs along channels running parallel to the *c*-direction in these hexagonal structures related to $CaCu_5$. A more closely related cubic example is found in the mixed fluoride 0.6 $BaLiF_3$ / 0.4 $NaCoF_3$ adopting a perovskite superstructure in which Na atoms (at 6*b*) are centred within a square of F atoms but are disordered with *A*–*A* dumbbells (*A* = Ba/Na, at 12*e*) skewering this square.[26]

The electrical resistivity of $Gd_{12}Co_{5.3}Bi$ shows very little dependence on temperature (as gauged by the residual resistivity ratio, ρ_{300K}/ρ_{5K} = 1.1) (Figure 9), consistent with the highly disordered nature of this compound. The data are relatively noisy, like arising from grain boundary effects or poor contacts, and the fine features in the resistivity curve are probably spurious. The absolute resistivity values are of similar magnitude (several hundred μΩ·cm) for $Gd_{12}Co_{5.3}Bi$ and $Gd_{12}Co_5Bi$. However, the temperature dependence of the resistivity for $Gd_{12}Co_{5.3}Bi$ lacks the downturn seen at low temperatures for $Gd_{12}Co_5Bi$ (as well as for the

closely related compound Gd_6Co_2Ga). This difference in behaviour provides further evidence that $Gd_{12}Co_{5.3}Bi$ is distinct from $Gd_{12}Co_5Bi$.

The heat capacity, thermal diffusivity, and thermal conductivity for both $Gd_{12}Co_{5.3}Bi$ and $Gd_{12}Co_5Bi$ are shown in Figure 10. Remarkably, the heat capacity for both compounds exhibits the highly unusual trend of *decreasing* from 0.3 J g^{-1} K^{-1} to 0.07 J g^{-1} K^{-1} over the temperature range from room temperature to 600 °C. In fact, whereas the expected heat capacity increases from zero to the Dulong-Petit limit of 3*R* as materials approach their Debye temperature, these compounds exhibit *opposite* behavior beginning approximately near the 3*R* value at room temperature and decreasing beyond even the 2*R* value that has been reported for liquids and a few unusual solids such as Cu_2Se.[27] In those cases, the liquid-like approximately 2*R* value for heat capacity was attributed to the highly disordered defected structure. The unusual heat capacities for $Gd_{12}Co_{5.3}Bi$ and $Gd_{12}Co_5Bi$ were repeatable on multiple samples and were measured on no less than three distinct DSC instruments at different institutions. We cannot completely rule out that small inclusions (<5 mol. %) visible in the samples studied could affect these properties, but the good consistency among different samples and different instruments strongly suggests that the behaviour is intrinsic. Although the heat capacity for both compounds starts and ends at approximately the same values, it decreases monotonically and smoothly for $Gd_{12}Co_{5.3}Bi$ whereas it seems to plateau near the 3*R* limit at intermediate temperatures for $Gd_{12}Co_5Bi$.

The thermal diffusivity for both $Gd_{12}Co_{5.3}Bi$ and $Gd_{12}Co_5Bi$ also shows a counterintuitive temperature dependence. Thermal diffusivity is defined as the ratio of how much heat is conducted through a substance to how much heat is stored in it. As such, thermal diffusivity generally shows a negative temperature dependence because conduction decreases

with higher temperature (increased scattering events) while heat capacity normally increases or approaches a plateau near the Dulong-Petit limit. However, in these compounds where we have experimentally observed that the heat capacity decreases with temperature, it is self-consistent that thermal diffusivity should in fact *rise* with temperature, which it does in linear fashion, approximately doubling from room temperature up to 600 ^{o}C.

The thermal conductivity, calculated from the measured heat capacity, thermal diffusivity, and density values for both compounds, shows remarkable difference at intermediate temperatures notwithstanding their similar crystal structures. $Gd_{12}Co_5Bi$ exhibits an increasing thermal conductivity trend with temperature over intermediate temperatures (with a slope, $d\kappa/dT$, of 0.006 $W\,m^{-1}\,K^{-2}$) consistent with the plateau in the heat capacity, whereas $Gd_{12}Co_{5.3}Bi$ exhibits a decreasing thermal conductivity trend (with a slope, $d\kappa/dT$, of –0.008 $W\,m^{-1}\,K^{-2}$). Beyond the plateau in the heat capacity, the thermal conductivity converges to the same low value of 2.8 $W\,m^{-1}\,K^{-1}$ for both compounds at high temperatures. This convergence is not surprising: at high temperatures, the phonon mean free path is already reduced, due to Umklapp scattering, to approximately the closest interatomic interactions, which are similar in these two compounds having nearly identical structures and compositions. At intermediate temperatures, however, the unusual opposite trends in thermal conductivity can be attributed to the subtle differences in the structures of the two compounds. $Gd_{12}Co_{5.3}Bi$ features a site splitting of Co atoms and Co–Co dumbbells, creating additional disorder at intermediate phonon wavelengths, which reduces thermal conductivity in this temperature range relative to the more ordered compound $Gd_{12}Co_5Bi$. Notably, although $Gd_{12}Co_{5.3}Bi$ and $Gd_{12}Co_5Bi$ are structural antitypes to the well-known filled and partially-filled skutterudites, they achieve their low thermal conductivity even without rattling occurring within cages.

4. Conclusions

Systematic investigation of the ternary Gd–Co–Bi system has led to definitive identification of a new phase $Gd_{12}Co_{5.3}Bi$ which differs subtly from the previously known phase $Gd_{12}Co_5Bi$. Despite their closeness in composition within the phase diagram, the best conditions to prepare them while minimizing the presence of other phases are to shift off-stoichiometry into three-phase regions so that slightly Co-rich compositions favour formation of $Gd_{12}Co_{5.3}Bi$ and slightly Co-poor compositions favour formation of $Gd_{12}Co_5Bi$. The difficulties in structural characterization of these phases – strong absorption effects, overlap of diffraction peaks, split sites – can be overcome by use of synchrotron radiation and by careful inspection of electron density maps. The key structural difference is that single Co atoms and Co–Co pairs are disordered within $Gd_{12}Co_{5.3}Bi$ but ordered within $Gd_{12}Co_5Bi$, which has important consequences to the physical properties. Both $Gd_{12}Co_{5.3}Bi$ and $Gd_{12}Co_5Bi$ exhibit several remarkable thermal properties. As the temperature increases, the heat capacity *decreases* beyond the 3*R* and even the 2*R* limit, while the thermal diffusivity *increases*; these trends are completely opposite to normal expectations. The thermal conductivities are quite low for both compounds (2.8 W m^{-1} K^{-1} at high temperatures), which is not typical for intermetallic phases. Moreover, the temperature dependence of the thermal conductivity shows opposite trends – decreasing for $Gd_{12}Co_{5.3}Bi$ and increasing for $Gd_{12}Co_5Bi$ – which can be attributed to the additional disorder introduced at intermediate phonon wavelengths for $Gd_{12}Co_{5.3}Bi$.

Table 1. Crystallographic Data for $Gd_{12}Co_{5.3}Bi$

Data collection and refinement	
formula	$Gd_{12}Co_{5.3(1)}Bi$
fw (amu)	2408.31
space group	$Im\bar{3}$ (No. 204)
a (Å)	9.713(6)
V (Å^3)	916(2)
Z	2
ρ_{calcd} (g cm^{-3})	8.728
T (K)	296(2)
crystal dimensions (mm)	0.06 × 0.06 × 0.03
radiation	graphite monochromated Mo $K\alpha$, λ = 0.71073 Å
μ(Mo $K\alpha$) (mm^{-1})	56.89
transmission factors	0.108–0.279
2θ limits	5.93–66.07°
data collected	$-14 \le h \le 14$, $-14 \le k \le 14$, $-14 \le l \le 14$
no. of data collected	6594
no. of unique data, including $F_o^2 < 0$	337 (R_{int} = 0.061)
no. of unique data, with $F_o^2 > 2\sigma(F_o^2)$	285
no. of variables	16
$R(F)$ for $F_o^2 > 2\sigma(F_o^2)$ [a]	0.049
$R_w(F_o^2)$ [b]	0.116
goodness of fit	1.094
$(\Delta\rho)_{max}$, $(\Delta\rho)_{min}$ (e Å^{-3})	4.10, –2.87
Positional and displacement parameters [c]	
Gd at 24g (0, y, z)	
y	0.19696(9)
z	0.30295(9)
U_{eq} (Å^2)	0.0272(3)

Co1 at 12*e* (*x*, 0, ½)	
occupancy	0.78(2)
x	0.1150(5)
U_{eq} (Å^2)	0.030(2)
Co2 at 6*b* (0, ½, ½)	
occupancy	0.22(2)
U_{eq} (Å^2)	0.032(6)
Bi at 2*a* (0, 0, 0)	
U_{eq} (Å^2)	0.0281(5)
Interatomic distances (Å)	
Gd–Co1	2.645(4)
Gd–Co2	2.706(2)
Gd–Co1 (×2)	2.928(3)
Gd–Co1	3.464(4)
Gd–Co2	3.511(2)
Gd–Gd (×4)	3.511(4)
Gd–Gd (×4)	3.658(4)
Gd–Bi	3.510(2)
Co1–Co1	2.234(11)
Co1–Gd (×2)	2.645(4)
Co1–Gd (×4)	2.928(3)
Co2–Gd (×4)	2.706(2)
Bi–Gd (×12)	3.510(2)

[a] $R(F) = \sum \left| |F_o| - |F_c| \right| / \sum |F_o|$.

[b] $R_w(F_o^2) = \left[\sum \left[w(F_o^2 - F_c^2)^2 \right] / \sum w F_o^4 \right]^{1/2}$; $w^{-1} = \left[\sigma^2(F_o^2) + (Ap)^2 + Bp \right]$ where $p = \left[\max(F_o^2, 0) + 2F_c^2 \right] / 3$.

[c] U_{eq} is defined as one-third of the trace of the orthogonalized U_{ij} tensor.

Table 2. Phases in Equilibria with $Gd_{12}Co_5Bi$ and $Gd_{12}Co_{5.3}Bi$ at 870 K

phase	EDX composition	structure type	space group	*a* (Å)	*b* (Å)	*c* (Å)
$Gd_{12}Co_5Bi$	$Gd_{70}Co_{24}Bi_6$	$Ho_{12}Co_5Bi$	*Immm*	9.585(1)	9.567(1)	10.030(1)
$Gd_{12}Co_{5.3}Bi$	$Gd_{67}Co_{28}Bi_5$	Own	$Im\bar{3}$	9.7184(9)		
Gd_5CoBi_2	$Gd_{68}Co_9Bi_{23}$	Y_2HfS_5	*Pnma*	12.244(3)	9.101(4)	8.026(2)
$Gd_6(Co_{1-x}Bi_x)_{4.5}$ (x = 0–0.15)	$Gd_{59}Co_{35}Bi_6$	$Ho_6Co_{4.5}$	$P6_3/m$	11.698(7)		4.029(6)
Gd_3Co	$Gd_{78}Co_{22}$	Fe_3C	*Pnma*	7.048(2)	9.541(2)	6.319(1)

Figure Captions

Figure 1. SEM image of $Gd_{12}Co_{5.3}Bi$ crystals grown on Gd_5CoBi_2 ingot.

Figure 2. Laboratory-based powder XRD patterns of (a) $Gd_{12}Co_5Bi$ and (b) $Gd_{12}Co_{5.3}Bi$ obtained with Cu *K*α radiation; a small unidentified peak in (b) is marked with an asterisk. Variable-temperature synchrotron powder XRD patterns of (c) $Gd_{12}Co_5Bi$ (λ = 0.413905 Å) and (d) $Gd_{12}Co_{5.3}Bi$ (λ = 0.459300 Å).

Figure 3. Phase diagram near the Gd corner of the Gd–Co–Bi system at 870 K.

Figure 4. Powder XRD patterns for some two-phase samples (labeled 3, 5, and 6 in the phase diagram shown in Figure 2) in the Gd–Co–Bi system obtained using laboratory-based Cu *K*α radiation (yellow) or synchrotron radiation with λ = 0.414208 Å (blue).

Figure 5. Cubic structure of $Gd_{12}Co_{5.3}Bi$ in terms of corner-sharing Gd_6 octahedra, Bi atoms, and disordered sets of Co1–Co1 dumbbells and single Co2 atoms. The grey lines outlining the octants of the unit cell are included to guide the eye.

Figure 6. (a) Model of disordered Co1–Co1 dumbbells and single Co2 atoms. (b) Electron density map in the vicinity of Co sites. (c) Magnified view of electron density map.

Figure 7. Structures of (a) $Gd_{12}Co_{5.3}Bi$ and (b) $RE_{12}Co_5Bi$ ($Ho_{12}Co_5Bi$-type) in terms of RE_4 squares centred by Co–Co dumbbells and single Co atoms. The actual unit cell is translated by ¼, ¼, ¼.

Figure 8. Group-subgroup relations between $Gd_{12}Co_{5.3}Bi$ and $Ho_{12}Co_5Bi$ structure types. For ease of comparison to $Gd_{12}Co_{5.3}Bi$ (*a* = 9.713(6) Å), the coordinates in $Ho_{12}Co_5Bi$ have been transformed after interchanging the *a* and *b* axes in the orthorhombic unit cell as originally reported (***a′*** = ***b*** = 9.3787(1) Å, ***b′*** = ***–a*** = 9.3760(1) Å, ***c′*** = ***c*** = 9.8546(1) Å).[2]

Figure 9. Electrical resistivity of $Gd_{12}Co_{5.3}Bi$ and $Gd_{12}Co_5Bi$. Data for $Gd_{12}Co_5Bi$ were taken from Ref. [2].

Figure 10. Heat capacity (top panel), thermal diffusivity (middle panel), and thermal conductivity (bottom panel) as a function of temperature for $Gd_{12}Co_5Bi$ and $Gd_{12}Co_{5.3}Bi$.

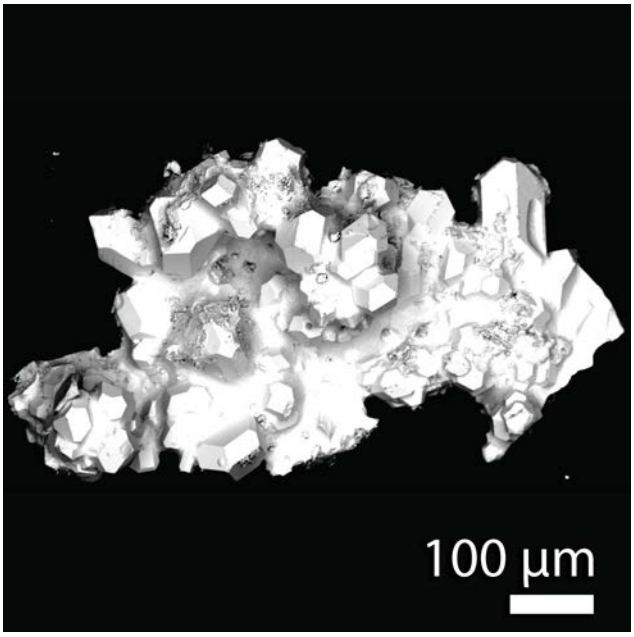

Figure 1. SEM image of $Gd_{12}Co_{5.3}Bi$ crystals grown on Gd_5CoBi_2 ingot.

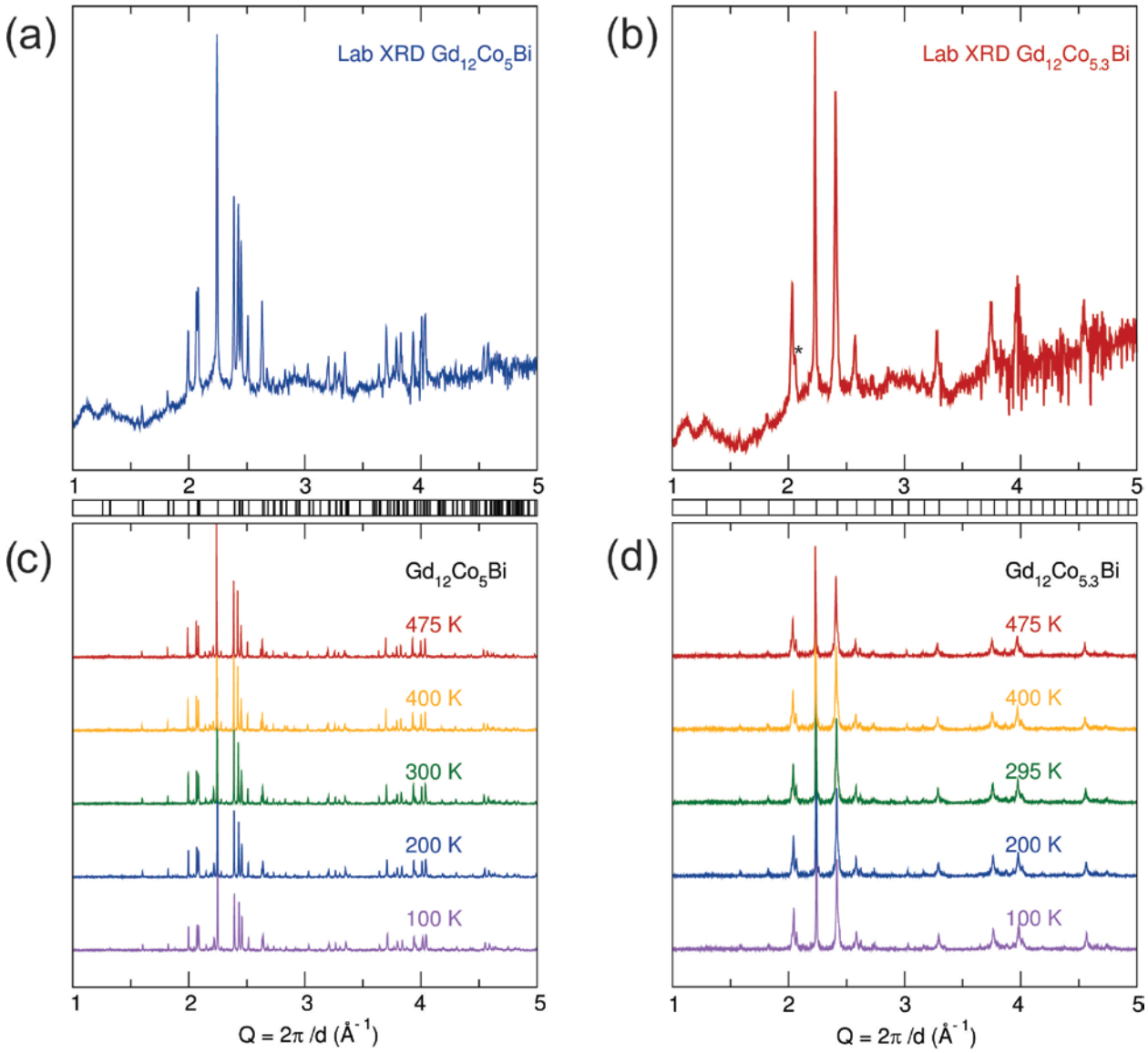

Figure 2. Laboratory-based powder XRD patterns of (a) $Gd_{12}Co_5Bi$ and (b) $Gd_{12}Co_{5.3}Bi$ obtained with Cu $K\alpha$ radiation; a small unidentified peak in (b) is marked with an asterisk. Variable-temperature synchrotron powder XRD patterns of (c) $Gd_{12}Co_5Bi$ (λ = 0.413905 Å) and (d) $Gd_{12}Co_{5.3}Bi$ (λ = 0.459300 Å).

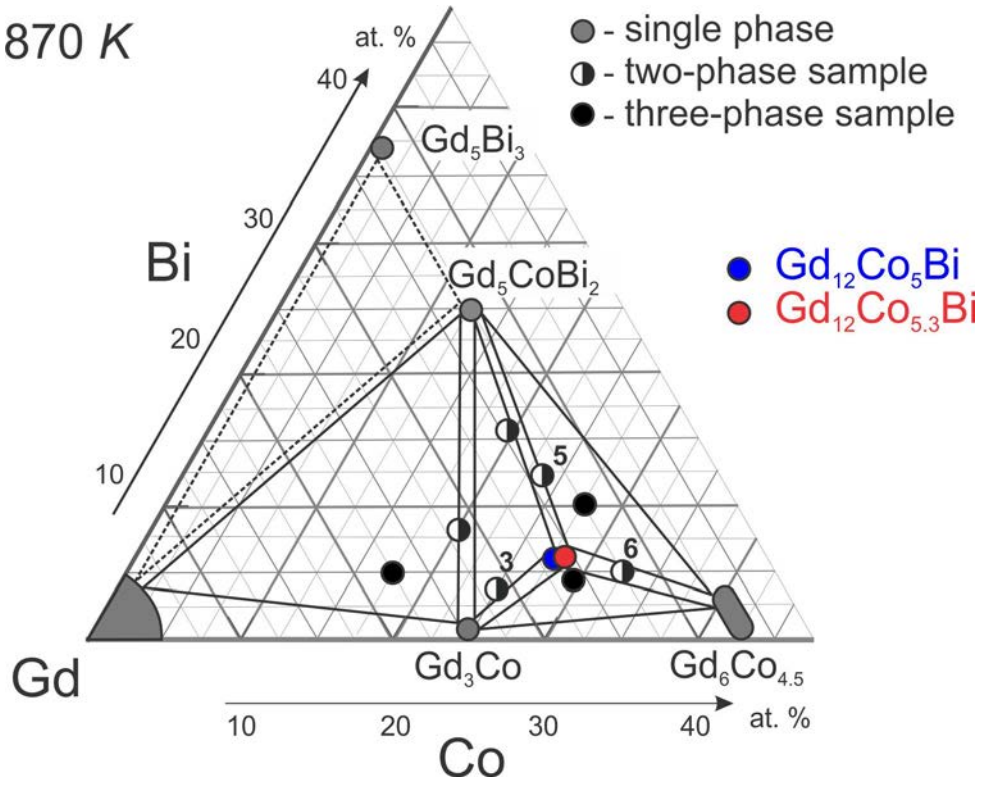

Figure 3. Phase diagram near the Gd corner of the Gd–Co–Bi system at 870 K.

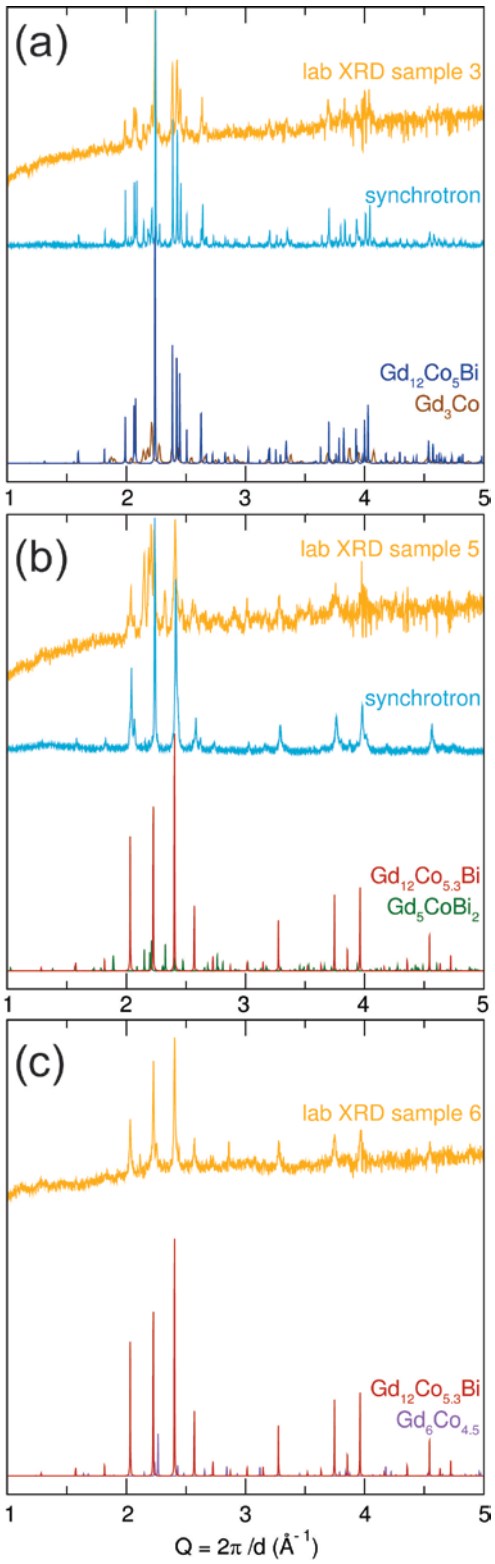

Figure 4. Powder XRD patterns for some two-phase samples (labeled 3, 5, and 6 in the phase diagram shown in Figure 2) in the Gd–Co–Bi system obtained using laboratory-based Cu *K*α radiation (yellow) or synchrotron radiation with λ = 0.414208 Å (blue).

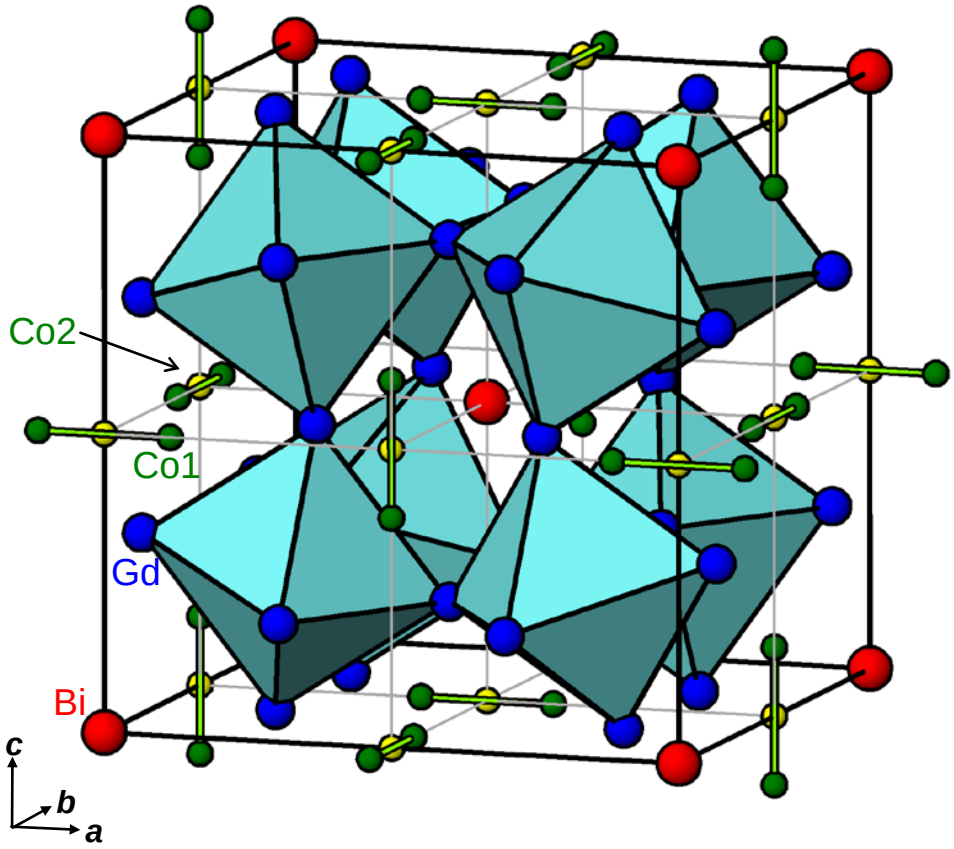

Figure 5. Cubic structure of $Gd_{12}Co_{5.3}Bi$ in terms of corner-sharing Gd_6 octahedra, Bi atoms, and disordered sets of Co1–Co1 dumbbells and single Co2 atoms. The grey lines outlining the octants of the unit cell are included to guide the eye.

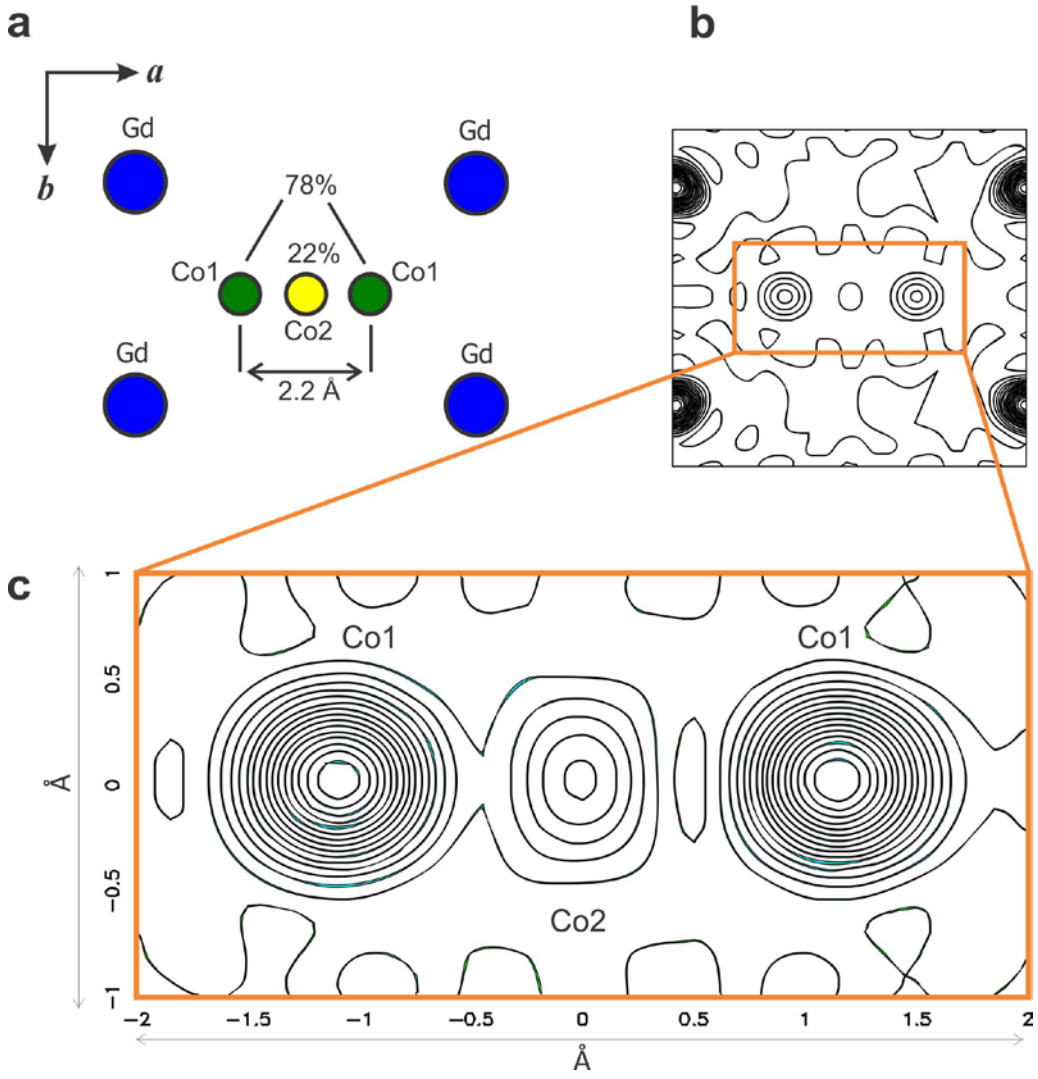

Figure 6. (a) Model of disordered Co1–Co1 dumbbells and single Co2 atoms. (b) Electron density map in the vicinity of Co sites. (c) Magnified view of electron density map.

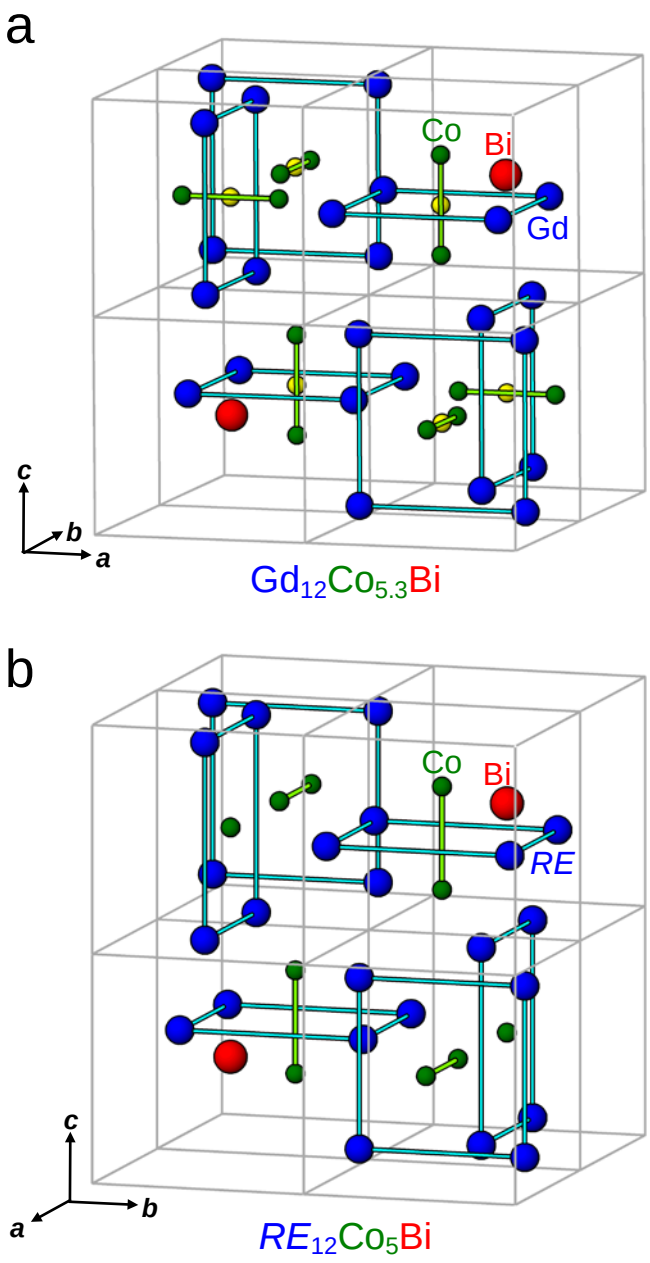

Figure 7. Structures of (a) $Gd_{12}Co_{5.3}Bi$ and (b) $RE_{12}Co_5Bi$ ($Ho_{12}Co_5Bi$-type) in terms of RE_4 squares centred by Co–Co dumbbells and single Co atoms. The actual unit cell is translated by ¼, ¼, ¼.

I 2/*m* $\bar{3}$

$Gd_{12}Co_{5.3}Bi$

t3

I 2/*m* 2/*m* 2/*m*

$Ho_{12}Co_5Bi$

Gd: 24*g*	0.78 Co: 12*e*	0.22 Co: 6*b*	Bi: 2*a*
m..	*mm*2..	*mmm*..	*m* $\bar{3}$.
0	0.385	0	0
0.197	½	½	0
0.303	0	½	0

Ho: 8*l*	Ho: 8*m*	Ho: 8*n*	□: 4*f*	Co: 4*h*	Co: 4*j*	□: 2*b*	Co: 2*d*	□: 2*c*	Bi: 2*a*
m..	.*m*.	..*m*	2*mm*	*m*2*m*	*mm*2	*mmm*	*mmm*	*mmm*	*mmm*
0	0.304	0.217	0.382	0	½	0	½	½	0
0.198	0	0.316	½	0.377	0	½	0	½	0
0.285	0.187	0	0	½	0.387	½	½	0	0

Figure 8. Group-subgroup relations between $Gd_{12}Co_{5.3}Bi$ and $Ho_{12}Co_5Bi$ structure types. For ease of comparison to $Gd_{12}Co_{5.3}Bi$ (*a* = 9.713(6) Å), the coordinates in $Ho_{12}Co_5Bi$ have been transformed after interchanging the *a* and *b* axes in the orthorhombic unit cell as originally reported (***a′*** = ***b*** = 9.3787(1) Å, ***b′*** = ***–a*** = 9.3760(1) Å, ***c′*** = ***c*** = 9.8546(1) Å).[2]

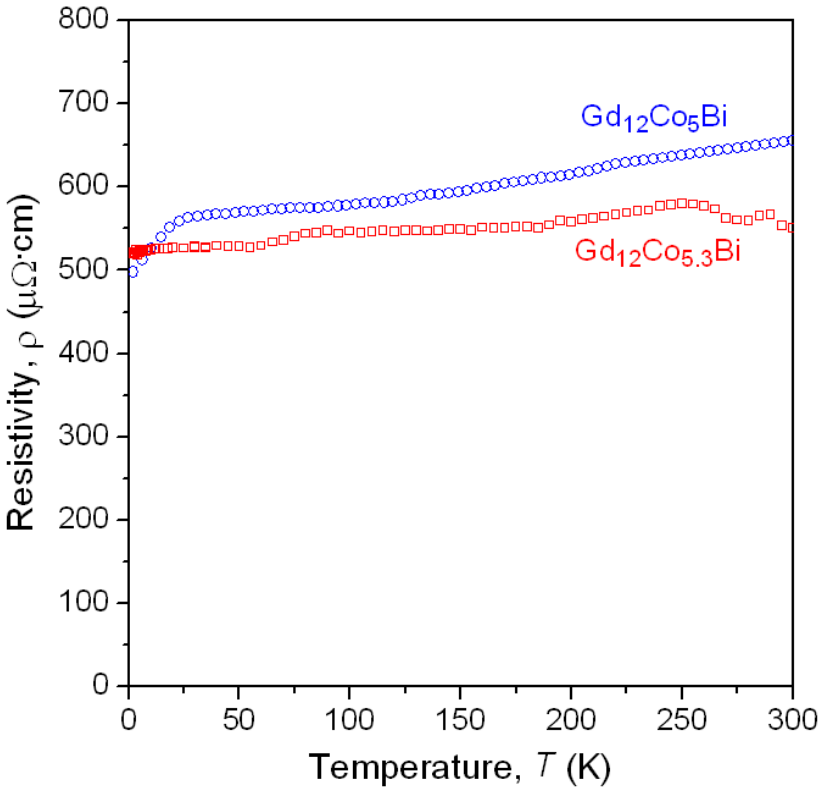

Figure 9. Electrical resistivity of $Gd_{12}Co_{5.3}Bi$ and $Gd_{12}Co_5Bi$. Data for $Gd_{12}Co_5Bi$ were taken from Ref. [2].

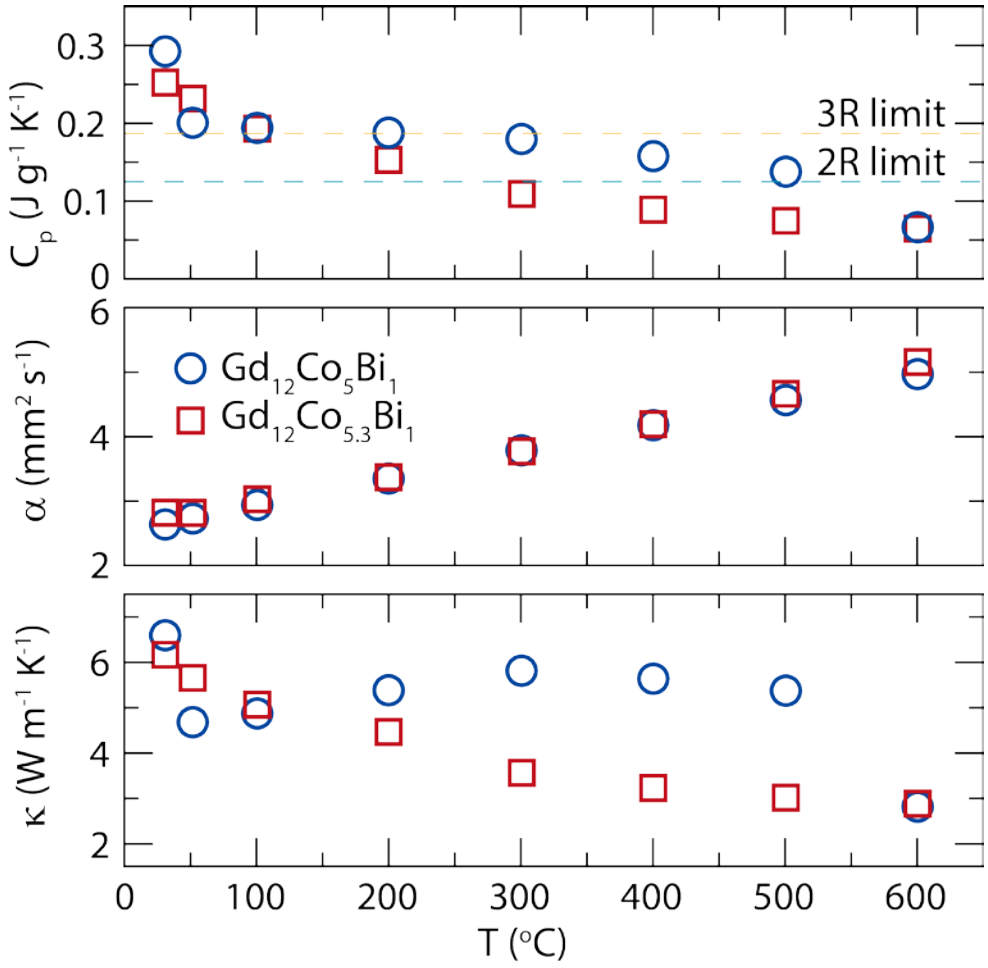

Figure 10. Heat capacity (top panel), thermal diffusivity (middle panel), and thermal conductivity (bottom panel) as a function of temperature for $Gd_{12}Co_5Bi$ and $Gd_{12}Co_{5.3}Bi$.

Associated Content

Supporting Information. X-ray crystallographic file in CIF format. This material is available free of charge via the Internet at http://pubs.acs.org or may be obtained from Fachinformationszentrum Karlsruhe, Abt. PROKA, 76344 Eggenstein-Leopoldshafen, Germany (No. CSD-431008).

Author Information

Corresponding Author

* E-mail: arthur.mar@ualberta.ca

Notes

The authors declare no competing financial interest.

Acknowledgment

This work was supported by the Natural Sciences and Engineering Research Council of Canada (NSERC) (AOO and AM). MWG is grateful for support from the European Union's Horizon 2020 research and innovation programme under the Marie Skłodowska-Curie grant agreement No. 659764. TDS also acknowledges resources from the DARPA SIMPLEX program N66001-15-C-4036. We thank Dr. Saul Lapidus for assistance with the high-resolution synchrotron X-ray diffraction experiments, made possible through the mail-in powder diffraction service, at 11-BM at the Advanced Photon Source at Argonne National Laboratory. Use of the Advanced Photon Source at Argonne National Laboratory was supported by the U.S. Department of

Energy, Office of Science, Office of Basic Energy Sciences, under Contract No. DE-AC02-06CH11357.

References

(1) Mar, A. In *Handbook on the Physics and Chemistry of Rare Earths*; Gschneidner, K. A., Jr., Bünzli, J.-C. G., Pecharsky, V. K., Eds.; Elsevier: Amsterdam, 2006; Vol. 36, pp 1–82.

(2) Tkachuk, A. V.; Mar, A. *Inorg. Chem.* **2005**, *44*, 2272–2281.

(3) Tkachuk, A. V.; Bie, H.; Mar, A. *Intermetallics* **2008**, *16*, 1185–1189.

(4) MacFarlane, W. A.; Chow, K. H.; Tkachuk, A. V.; Mar, A.; Russo, P. L.; Smadella, M.; Song, Q.; Xu, M.; Hitti, B.; Arseneau, D. J. *J. Phys. Chem. C* **2007**, *117*, 5526–5532.

(5) Egilmez, M.; Chow, K. H.; MacFarlane, W. A.; Mar, A.; Fan, I.; Mansour, A.; Schlick-Martin, D.; Jung, J.; Tkachuk, A. V.; Hitti, B.; Arseneau, D. J. *J. Appl. Phys.* **2009**, *105*, 07A906-1–07A906-3.

(6) Egilmez, M.; Fan, I.; Chow, K. H.; MacFarlane, W. A.; Mansour, A. I.; Martin, D. S.; Jung, J.; Hitti, B.; Arseneau, D. J.; Tkachuk, A. V.; Mar, A. *Physica B* **2009**, *404*, 611–614.

(7) Egilmez, M.; Chow, K. H.; MacFarlane, W. A.; Salman, Z.; Mar, A.; Fan, I.; Jung, J.; Bie, H.; Tkachuk, A. V.; Schick-Martin, D.; Hitti, B.; Arseneau, D. *J. Supercond. Nov. Magn.* **2015**, *28*, 2597–2603.

(8) Gaultois, M. W.; Oliynyk, A. O.; Mar, A.; Sparks, T. D.; Mulholland, G. J.; Meredig, B. arXiv:1502.07635 [cond-mat.mtrl-sci].

(9) Roberts, N. A.; Walker, D. G. *Int. J. Therm. Sci.* **2011**, *50*, 648–662.

(10) "*He's another person, your Excellency, and I'm another person too; he's apart and I am myself by myself too; I am really myself by myself, your Excellency, really myself by myself.*" Dostoyevsky, F. M. (Transl. Garnett, C.) *The Double: A Petersburg Poem*, 1846.

(11) Sheldrick, G. M. *SHELXTL*, version 6.12; Bruker AXS Inc.: Madison, WI, 2001.

(12) Villars, P.; Cenzual K. *Pearson's Crystal Data – Crystal Structure Database for Inorganic Compounds (on DVD)*, Release 2015/16; ASM International, Materials Park, OH, USA.

(13) Cape, J. A.; Lehman, G. W. *J. Appl. Phys.* **1963**, *34*, 1909–1913.

(14) Oftedal, I. *Z. Kristallogr.* **1928**, *66*, 517–546.

(15) Rundqvist, S.; Ersson, N. O. *Ark. Kemi* **1968**, *30*, 103–114.

(16) Kjekshus, A.; Rakke, T. *Acta Chem. Scand. A* **1974**, *28*, 99–103.

(17) Jeitschko, W.; Braun, D. *Acta Crystallogr., Sect. B* **1977**, *33*, 3401–3406.

(18) Müller, U. *Symmetry Relationships between Crystal Structures*; Oxford University Press: Oxford, 2013.

(19) Gladyshevskii, R. E.; Grin', Yu. M.; Yarmolyuk, Ya. P. *Dopov. Akad. Nauk Ukr. RSR, Ser. A: Fiz.-Mat. Tekh. Nauki* **1983**, *2*, 67–70.

(20) Kalychak, Ya. M.; Zaremba, V. I.; Stępień-Damm, A.; Galadzhun, Ya. V.; Aksel'rud, L. G. *Crystallogr. Rep.* **1998**, *43*, 12–15.

(21) Mozharivkskyj, Yu.; Franzen, H. F. *J. Solid State Chem.* **2000**, *152*, 478–485.

(22) Demchyna, M.; Belan, B.; Manyako, M.; Akselrud, L.; Gagor, A.; Dzevenko, M.; Kalychak, Ya. *Intermetallics* **2013**, *37*, 22–26.

(23) Kripyakevich, P. I.; Frankevich, D. P.; Zarechnyuk, O. S. *Visn. Lviv. Derzh. Univ., Ser. Khim.* **1965**, *8*, 61–74.

(24) Buschow, K. H. J. *J. Less-Common Met.* **1966**, *11*, 204–208.

(25) Mills, A. M.; Mar, A. *J. Alloys Compd.* **2000**, *298*, 82–92.

(26) Welsch, M.; Kummer-Dörner, S.; Peschel, B.; Babel, D. *Z. Anorg. Allg. Chem.* **1999**, *625*, 1255–1260.

(27) Liu, H.; Shi, X.; Xu, F.; Zhang, L.; Zhang, W.; Chen, L.; Li, Q.; Uher, C.; Day, T.; Snyder, G. J. *Nat. Mater.* **2012**, *11*, 422–425.

For Table of Contents Only

$Gd_{12}Co_{5.3}Bi$ and $Gd_{12}Co_5Bi$ with similar compositions are distinct phases exhibiting an order-disorder structural relationship. Their thermal properties are unusual, including low thermal conductivities atypical for intermetallic compounds.

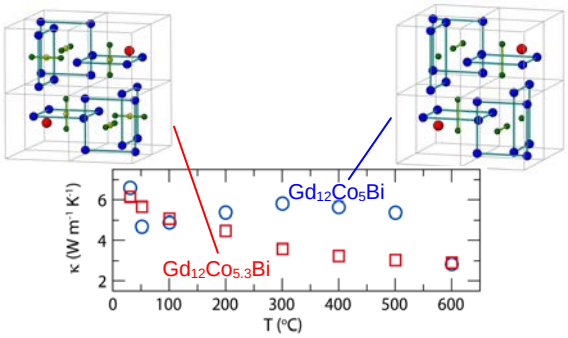

SUPPORTING INFORMATION

$Gd_{12}Co_{5.3}Bi$ and $Gd_{12}Co_5Bi$, Crystalline Doppelgänger with Low Thermal Conductivities

Anton O. Oliynyk,[†] Taylor D. Sparks,[‡] Michael W. Gaultois,[§] Leila Ghadbeigi,[‡] and Arthur Mar[†,*]

[†] *Department of Chemistry, University of Alberta, Edmonton, AB T6G 2G2 Canada*

[‡] *Department of Materials Science and Engineering, University of Utah, Salt Lake City, UT 84112 USA*

[§] *Department of Chemistry, University of Cambridge, Cambridge CB2 1EW United Kingdom*

Figure S1. SEM/EDX analysis of polished samples of (a) $Gd_{12}Co_5Bi$ and (b) $Gd_{12}Co_{5.3}Bi$.

Figure S2. Rietveld fits to powder XRD patterns of (a) $Gd_{12}Co_5Bi$ and (b) $Gd_{12}Co_{5.3}Bi$.

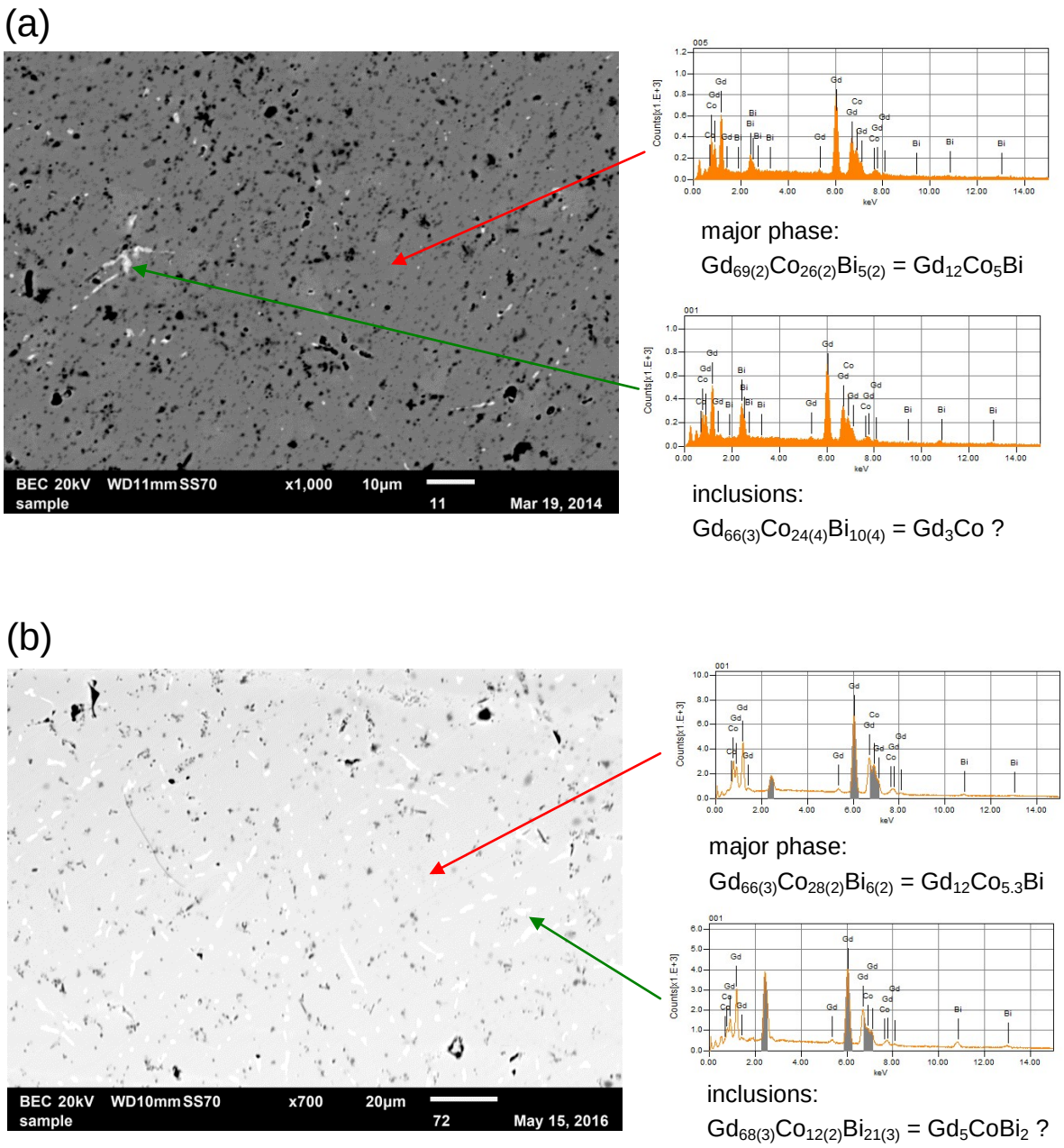

Figure S1. SEM/EDX analysis of polished samples of (a) $Gd_{12}Co_5Bi$ and (b) $Gd_{12}Co_{5.3}Bi$.

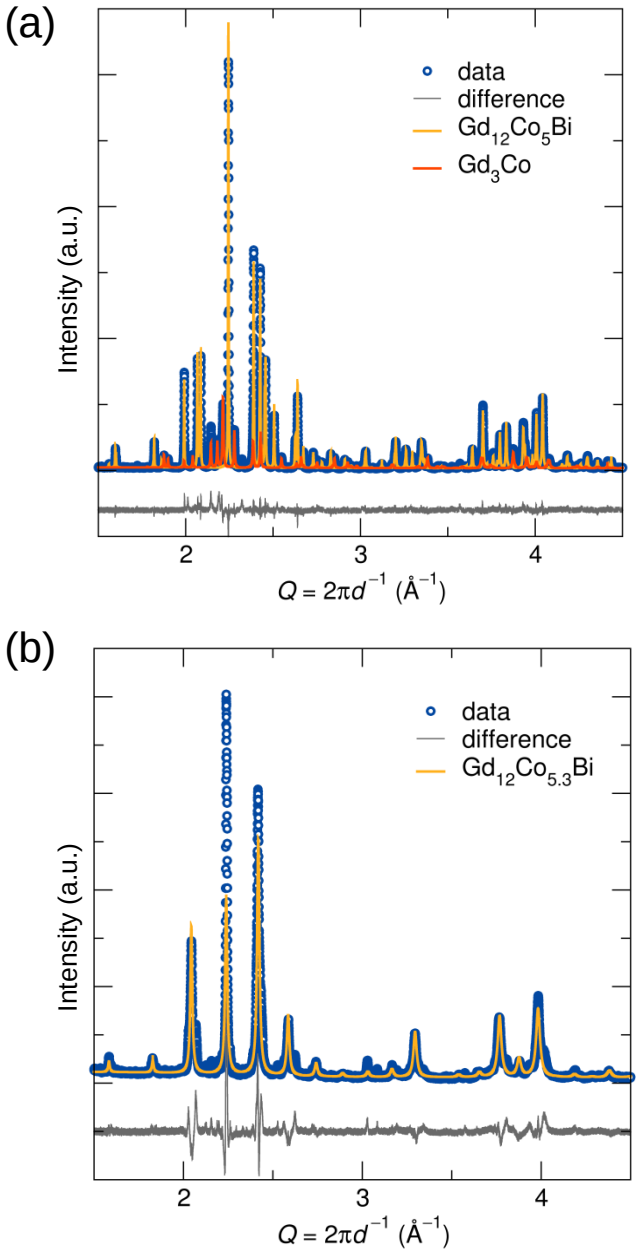

Figure S2. Rietveld fits to powder XRD patterns of (a) $Gd_{12}Co_5Bi$ and (b) $Gd_{12}Co_{5.3}Bi$.